

Supplementary Information

Hybrid Plasmonic Au-TiN Vertically Aligned Nanocomposites: A Nanoscale Platform towards Tunable Optical Sensing

*Xuejing Wang¹, Jie Jian¹, Susana Diaz Amaya¹, Cindy E. Kumah³, Ping Lu⁴, Jijie Huang¹, Daw
Gen Lim¹, Vilas Pol², Jeffrey Youngblood¹, Alexandra Boltasseva⁵, Lia Stanciu¹, Deirdre
O'Carroll³, Xinghang Zhang¹, Haiyan Wang^{1,5*}*

¹Department of Materials Engineering, Purdue University, West Lafayette, Indiana 47907, USA

²Department of Chemical Engineering, Purdue University, West Lafayette, Indiana 47907, USA

³Department of Materials Science and Engineering, Rutgers University, Piscataway, New Jersey
08854, USA

⁴Sandia National Laboratories, Albuquerque, New Mexico 87185, USA

⁵Department of Electrical Engineering, Purdue University, West Lafayette, Indiana 47907, USA

* To whom correspondence should be addressed. E-mail: hwang00@purdue.edu

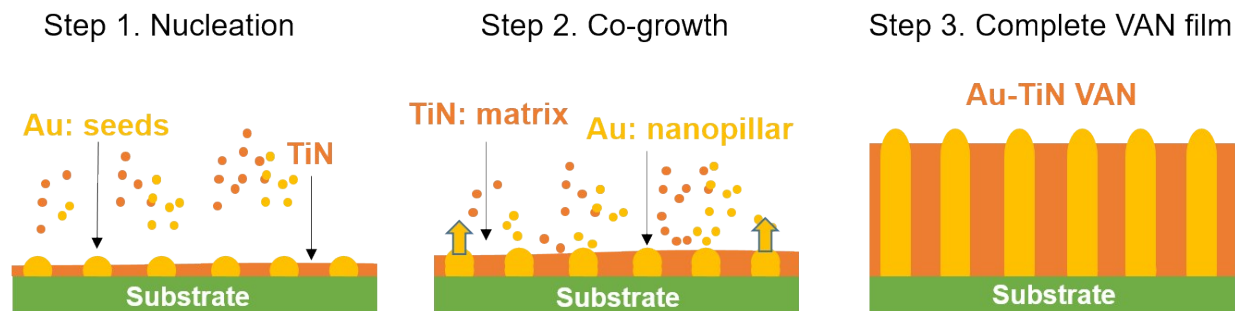


Figure S1| Growth mechanism of Au-TiN vertically aligned nanocomposite (VAN). Step1: Au nucleation as small islands as seed layer. Step 2: TiN and Au co-growth of initial VAN layer, TiN forms the matrix layer and Au nucleates on top of the seed layer forming nanopillars. Step 3: Completed VAN film, with smooth surface and protruded Au nanopillars.

Figure S1 discussion:

The initial nucleation is the key of growth morphology for the Au-TiN hybrid thin films. Au has a higher surface energy, and it nucleates as small islands as the Au nucleus. Here, the Au island spacing is mainly controlled by the Au density in the target. TiN grows as the matrix as it favors the layered growth. As the growth continues, the Au adatoms stack on top of each other. The high kinetic energy during growth plays a role in forming straight pillars and limit the lateral diffusion of the adatoms. In addition, the strain between the Au and TiN phases and the substrate MgO also play a role in the overall arrangement of the Au nanopillars. TiN ($a=4.24 \text{ \AA}$) presents a nearly perfect lattice match on MgO ($a=4.21 \text{ \AA}$) with a minor in-plane compressive strain, while Au ($a=4.065 \text{ \AA}$) presents an in-plane tensile strain on MgO. The possible in-plane strain compensation among the Au nanopillars and the TiN matrix also plays a role in the overall pillar distribution on the substrate.

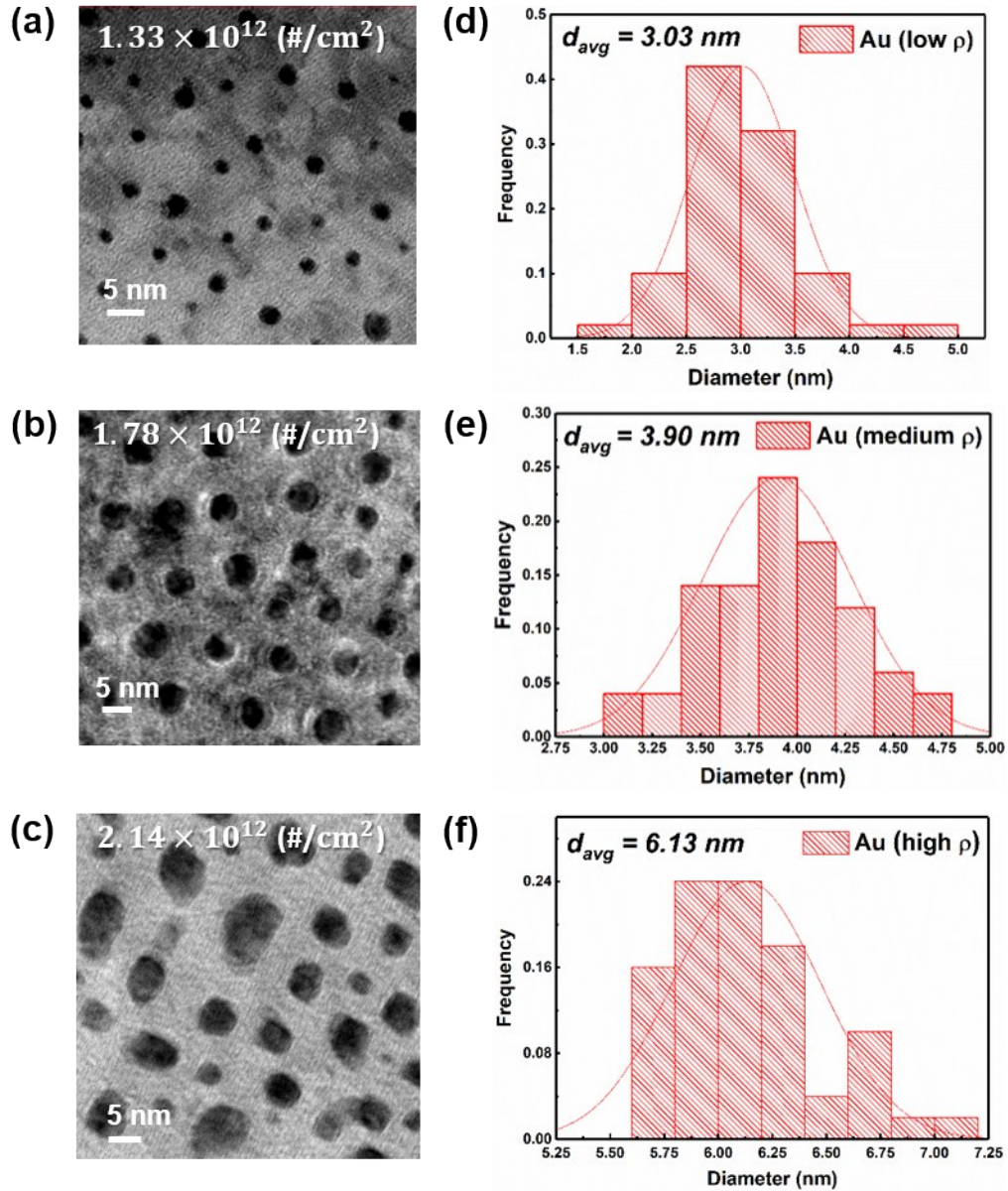


Figure S2| Quantification of metasurface Au density. (a-c) Plan-view TEM images and their calculated density expressed by number of nanopillars per centimeter square (#/cm²). (d-f) Au diameter quantified from the corresponding TEM plan view images, shown as bar plots, which indicate nanopillar widening as Au density increases. In general, the diameter can be controlled within 10 nm, and the overall volume fractions of nanopillar densities are gradually tuned.

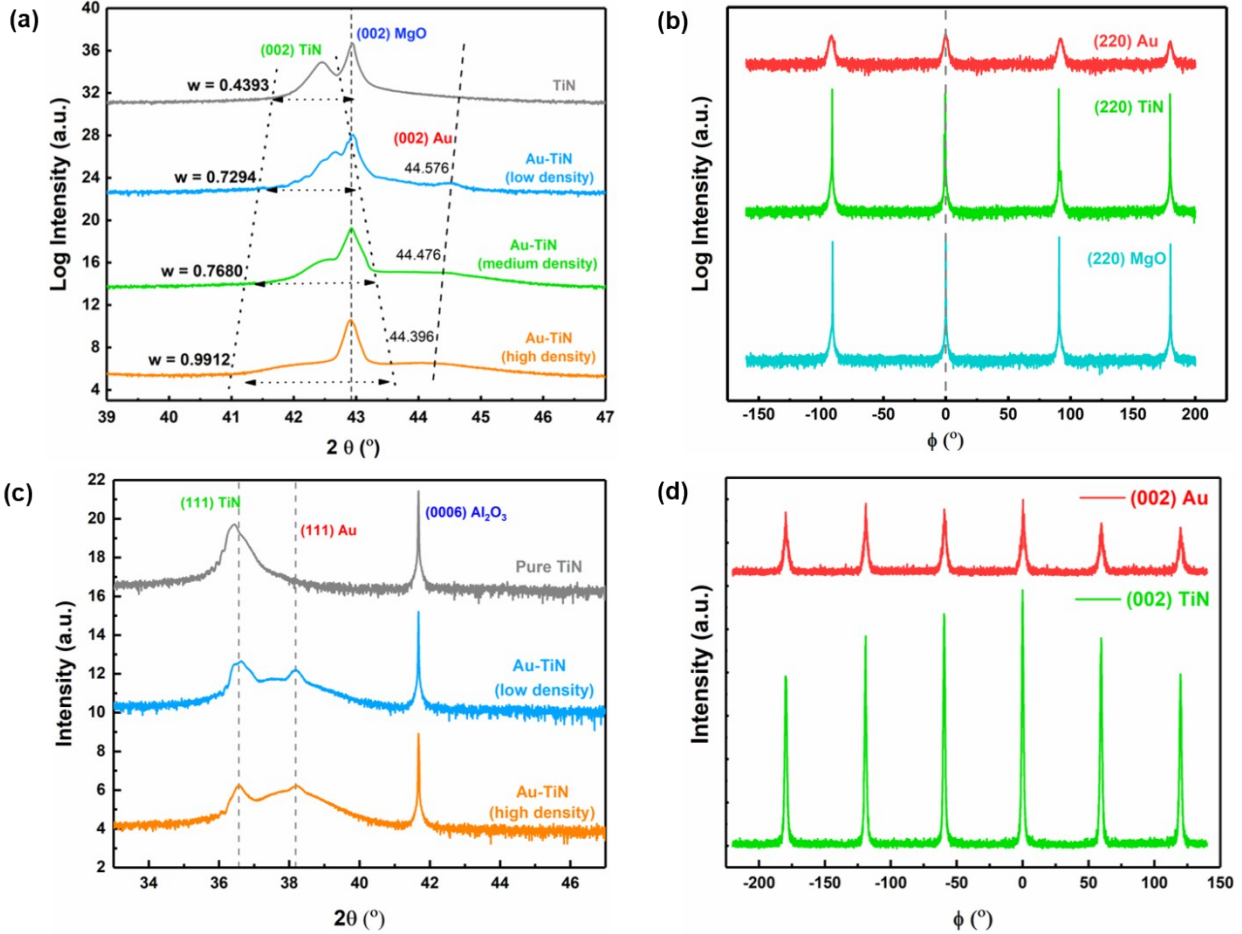


Figure S3| X-ray diffraction results. (a) θ - 2θ scans of density tuned Au-TiN nanocomposites versus a pure TiN for reference. A general widening of (002) TiN peak and continuous increase of (002) d-spacing is observed with increase of Au density. (b) Phi scan of Au-TiN on MgO substrate, indicating a four-fold symmetry without in-plane rotations. (c) θ - 2θ scans of the samples grown on (0001) sapphire substrates, with films oriented as (111) for better lattice match. (d) Phi scan of films grown on sapphire, indicating a hexagonal (six-fold) symmetry of (111) Au and (111) TiN.

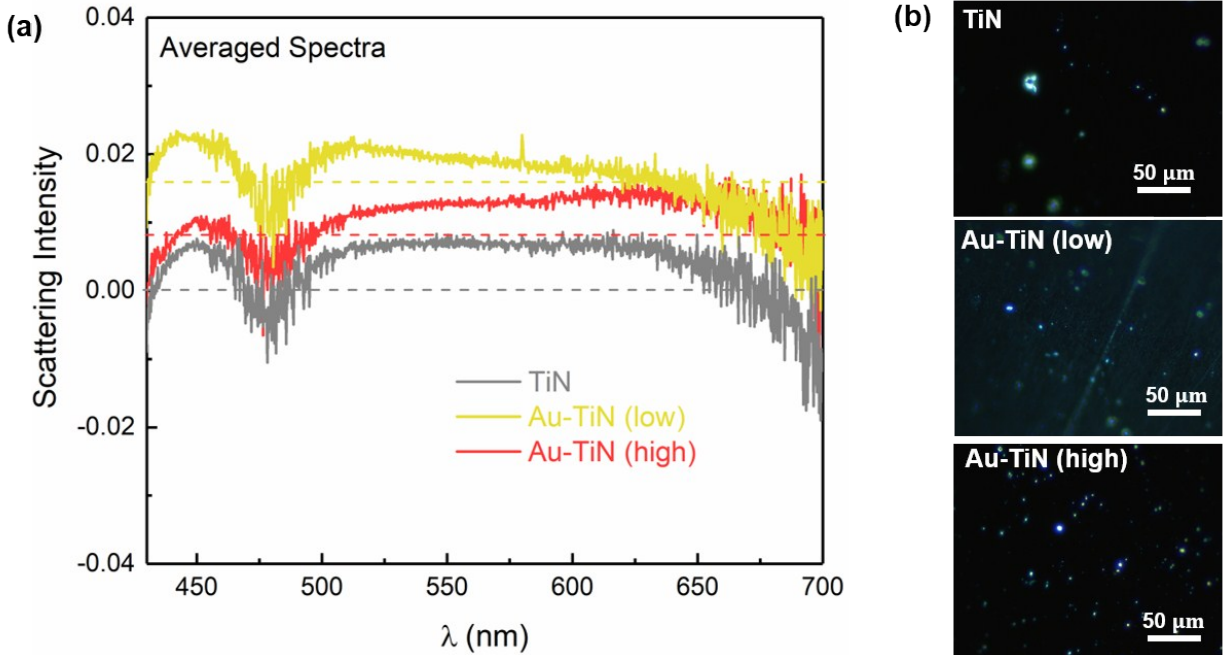


Figure S4| (a) Surface scattering intensity of three samples. The scattering intensity of the three samples are too low to contribute significantly to the reflectance signals, indicating high specular reflectance from the smooth metasurfaces. **(b)** Dark-field optical imaging of three thin film samples: pure TiN, low density Au-TiN and high density Au-TiN. The bright spots are attributed to micron-scale surface defects or agglomerations.

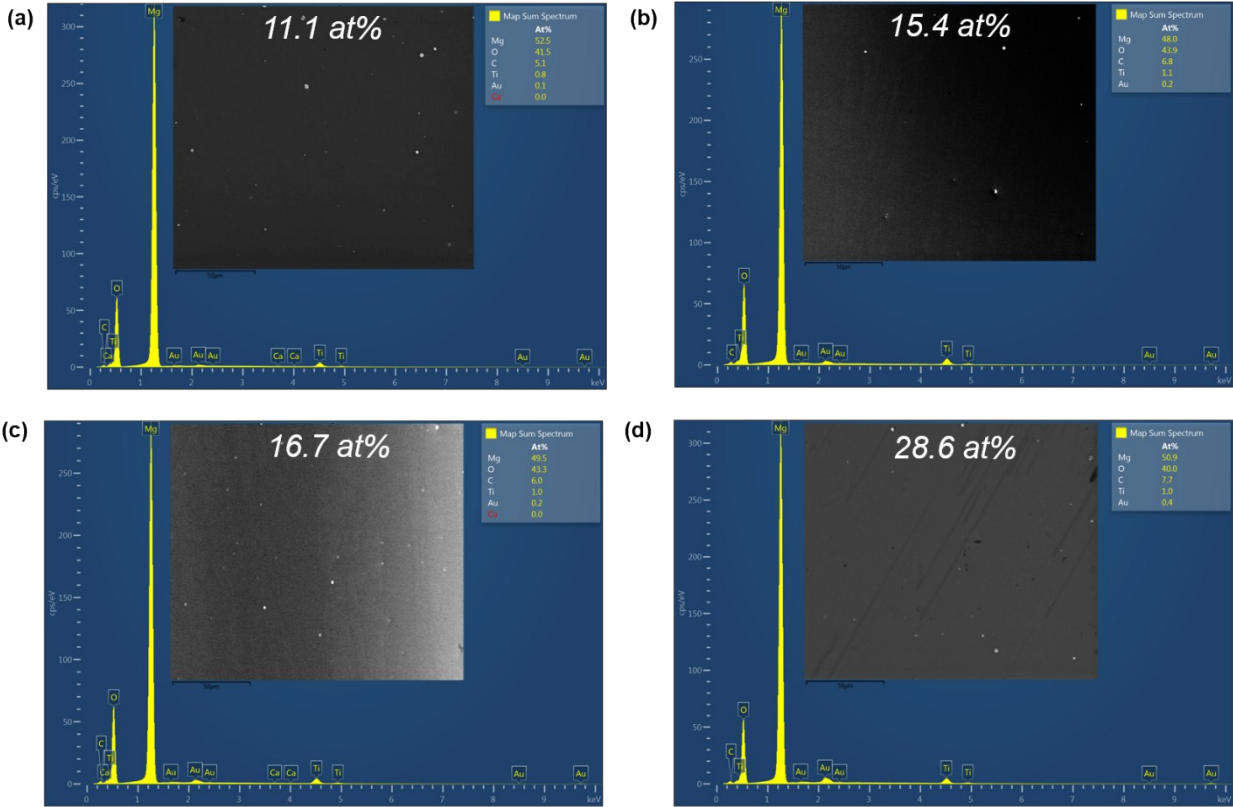


Figure S5 | EDS mapping of critical elements from a large scale for atomic percentage quantification of Au nanopillars in the TiN matrix. Atomic percentage of elements (Mg, O, C, Ti, Au) are shown at top corner. Insets are SEM images which confirm smooth surfaces of the Au-TiN/MgO samples, with quantified Au densities: **(a)** 11.1 at%, **(b)** 15.4 at%, **(c)** 16.7 at% and **(d)** 28.6 at% Au at%

Au density calculation is carried using: $\rho_{Au\ at\%} = \frac{Au\ at\%}{Au\ at\% + Ti\ at\%}$.

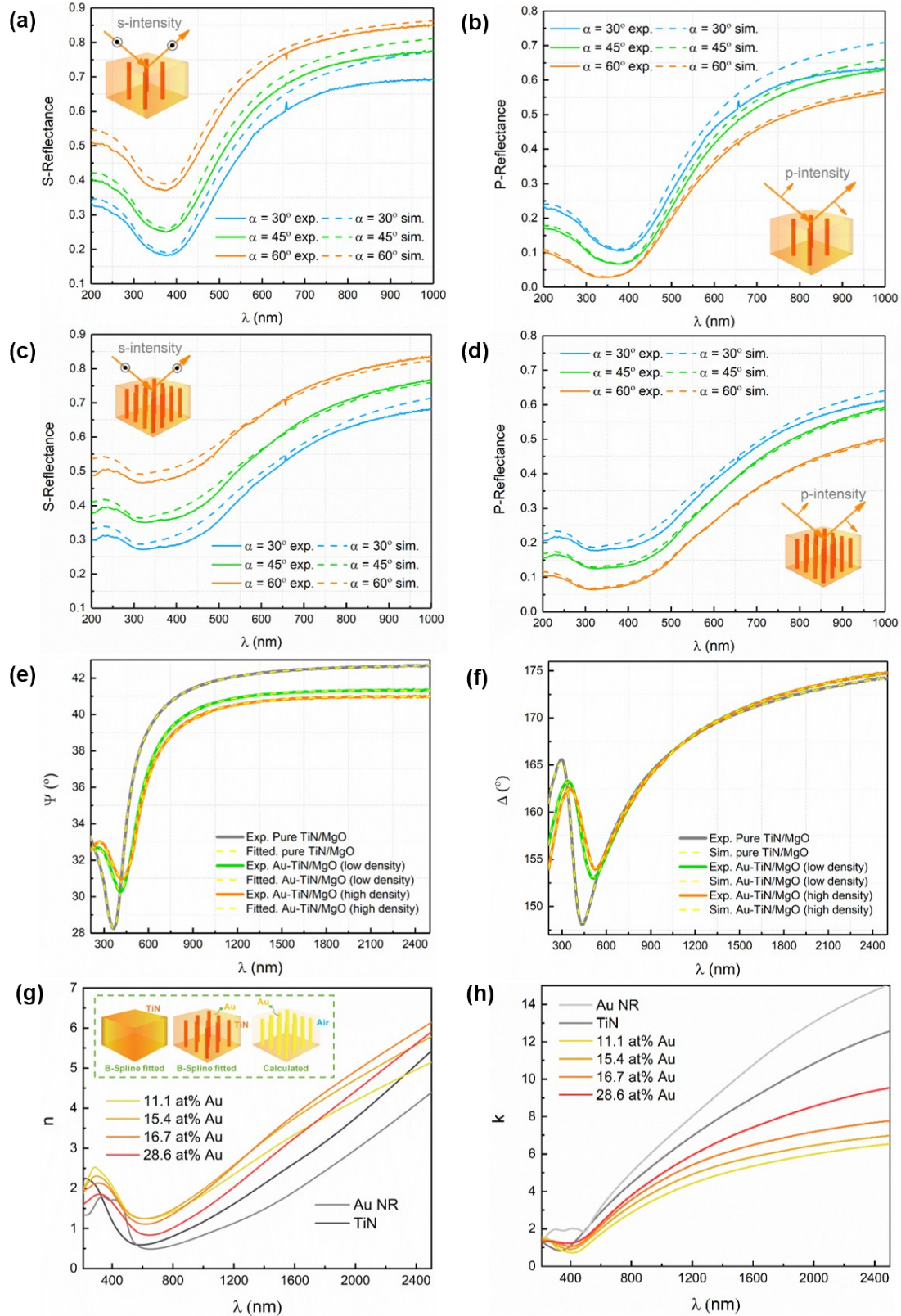


Figure S6] Angular dependent reflectance intensities for both s- and p-polarized light excitations of (a-b) low density Au-TiN, and (c-d) high-density Au-TiN. Three angles including 30, 45, and 60 degrees were selected for measurements. Note that the trend of the s- and p-polarized spectra

as a function of the incident angle is opposite. Because s-polarized light vibrates mainly parallel to the surface, the overall reflectance signal increases at more oblique incidence. However, the TM (p-polarized) tensor propagating into the film induces stronger surface plasmon polaritons (SPPs) at metasurface/air interface as well as Au nanopillar/TiN interfaces, therefore showing enhanced reflectance intensity at larger angles of incidence. **(e)** Psi and **(f)** delta ellipsometric and fitted parameters of pure TiN and Au-TiN nanocomposites. Optical constants are retrieved using B-Spline models, which specifies optical constants versus wavelength using a series of control points (nodes) which are equally spaced in photon energy (eV), detailed theory is described elsewhere (Cheney and Kincaid, "Numerical Mathematics and Computing," Third Edition, Brooks/Cole Publishing Company 1994). Averaged mean square error (MSE) in this model is 0.842, indicating a desired match between experimental and fitted data. **(g)** Refractive index and **(h)** extinction coefficient of Au nanorods (calculated), pure TiN film and four Au-TiN films with different Au densities. The extinction coefficient at higher wavelength range indicates lower losses of Au-TiN hybrids as compared to pure Au or TiN films.

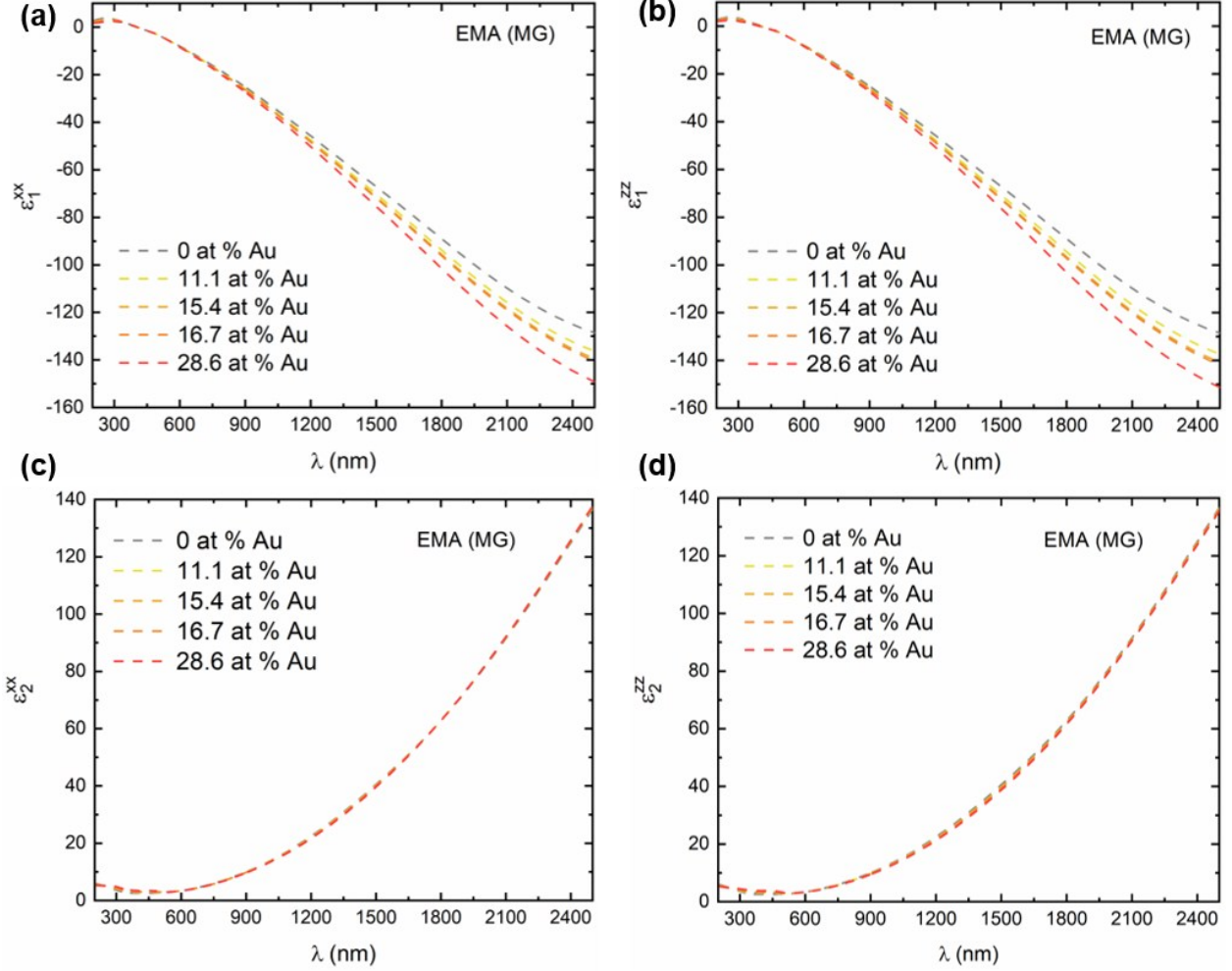


Figure S7 | Anisotropic effective permittivity as a function of Au densities in Au-TiN hybrid thin films. **(a)** In plane (ordinary) real part dielectric constant, **(b)** out-of-plane (extra-ordinary) real part dielectric constant, **(c)** in plane imaginary part dielectric constant, and **(d)** out-of-plane imaginary part dielectric constant. Results are calculated from effective medium theory Maxwell-Garnett (MG) method:

$$\epsilon_{xx, yy} = \frac{A\epsilon_{Au}\epsilon_{TiN} + (1-A)\epsilon_{TiN}[\epsilon_{TiN} + \frac{1}{2}(\epsilon_{Au} - \epsilon_{TiN})]}{A\epsilon_{TiN} + (1-A)[\epsilon_{TiN} + \frac{1}{2}(\epsilon_{Au} - \epsilon_{TiN})]} \quad \text{and}$$

$$\epsilon_{zz} = A\epsilon_{Au} + (1-A)\epsilon_{TiN},$$

where A is the area fraction of the Au nanopillars, which is calculated according to the atomic percentage of Au quantified from SEM, ϵ_{Au} and ϵ_{TiN} are wavelength dependent dielectric functions of Au and TiN, respectively, ϵ_{xx} , ϵ_{yy} are in-plane (ordinary) dielectric constants, while ϵ_{zz} is the out-of-plane (extraordinary) dielectric constant. The Maxwell-Garnett method is used

here due to the dilute and well-separated Au nanopillars, with densities ranging from 11.1 at% to 28.6 at%.

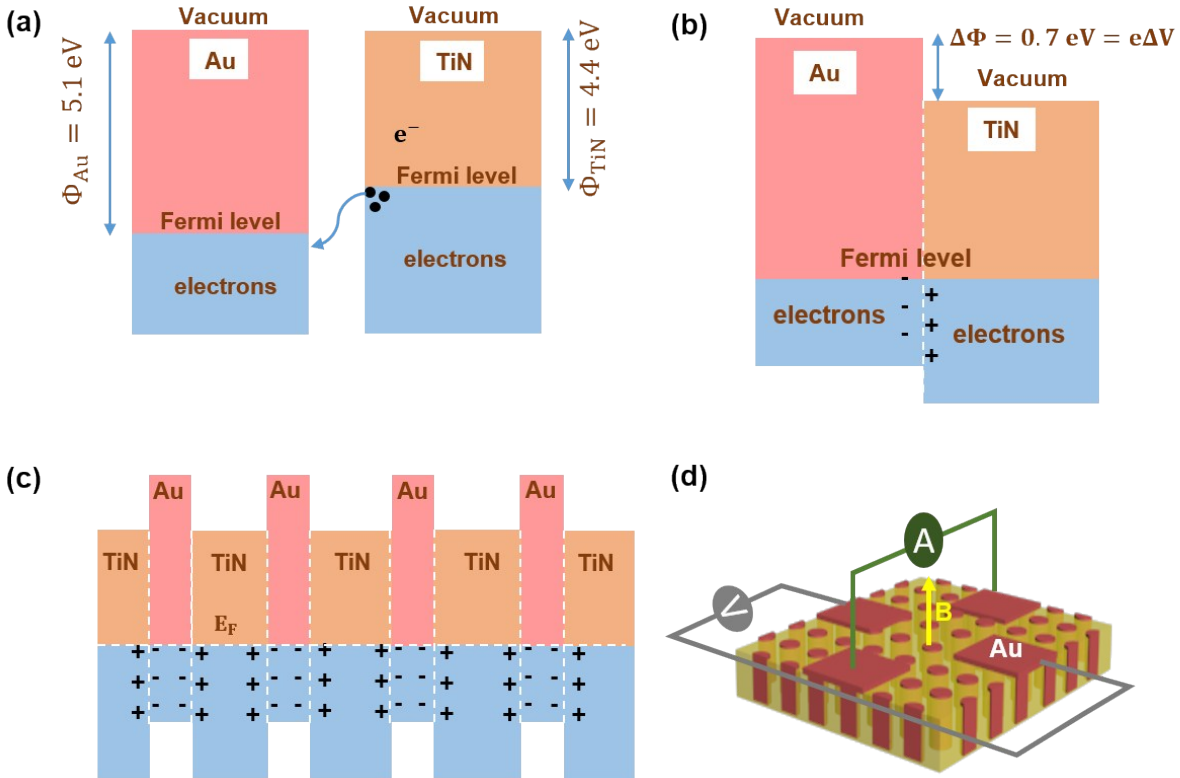


Figure S8 | (a-c) Proposed band diagram at Au-TiN junction, and the predicted electron density profile at nanocomposite cross-section. Bulk Au and TiN have a work function of 5.1 eV and 4.4 eV, respectively. At the metallic junction (boundaries) between Au and TiN, there could be electron density variances that electrons accumulated at the Au side while holes at the TiN side. Overall, the Au-TiN nanocomposites are showing enhanced charge carrier density with increased Au nanopillar densities. (d) Experimental setup of Hall measurements.

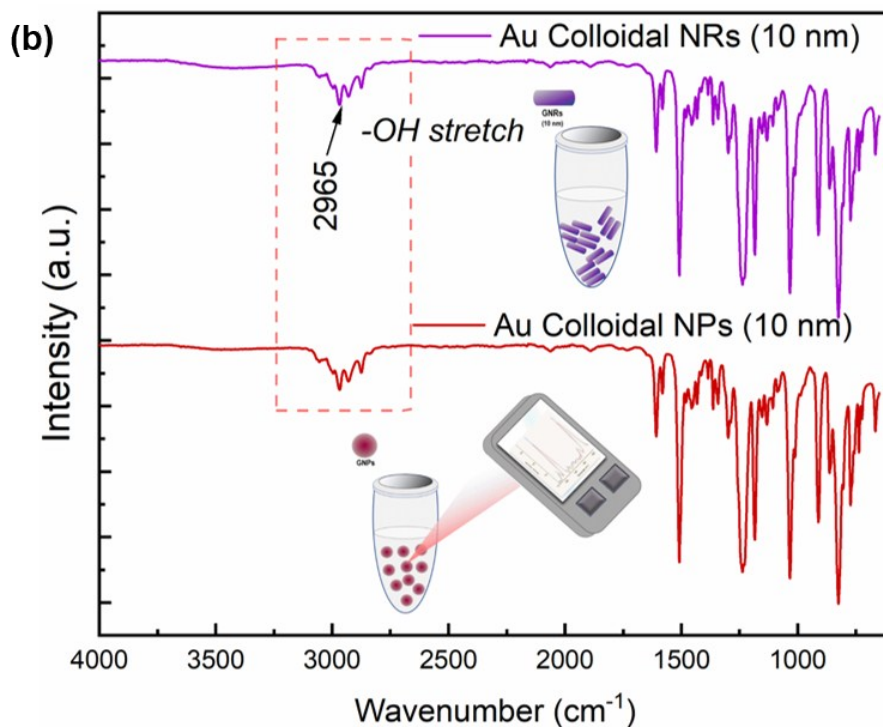
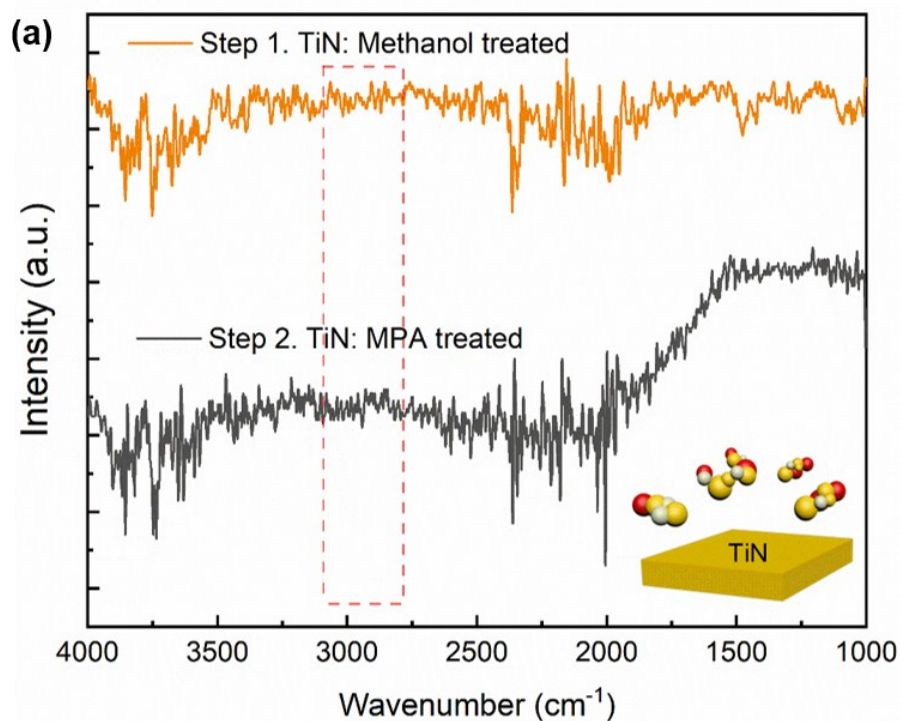


Figure S9] Total internal reflection FTIR spectra from reference samples. Following the similar procedure, the samples were washed with chemicals ($-\text{OH}$) before collecting the spectra. (a) Spectra of pure TiN films from the first two steps, showing no interaction with $-\text{OH}$ stretch.

(b) Spectra of Au colloidal nanoparticles (NPs) and nanorods (NPs) with diameter of 10 nm. Both shows the -OH stretching at $\sim 2965 \text{ cm}^{-1}$.

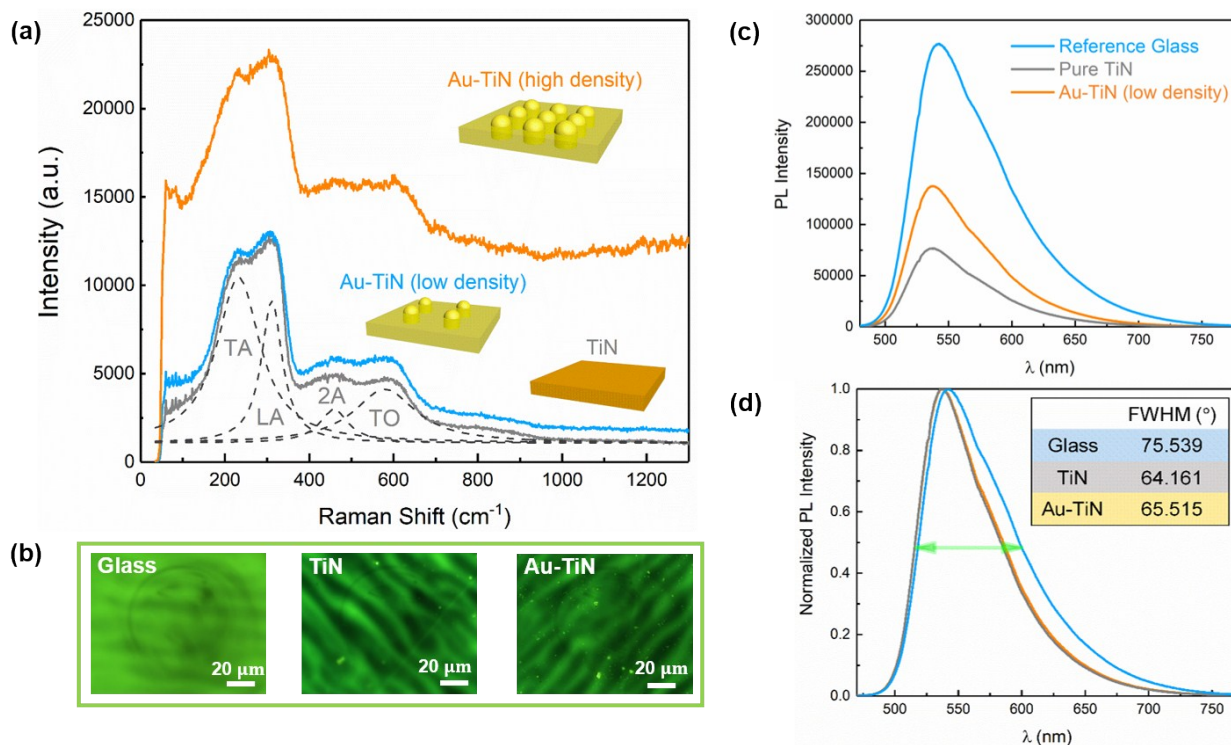


Figure S10 | (a) Raman spectra of pure TiN, low and high density Au-TiN thin films. Enhancement on SERS signals shown as overall increase of spectrum intensity. First-order transverse acoustic (TA), longitudinal acoustic (LA), transverse optical (TO) and the second-order acoustic (2A) modes maintain comparable in Au-TiN nanocomposites and match with reported values of TiN, indicating a 1:1 ratio of TiN while introducing Au phase. (b) Fluorescence (PL) images and (c-d) PL intensities and their normalized spectra excited at 365 nm for three samples: a reference glass, a pure TiN and an Au-TiN samples with spin-coated fluorescent conjugated polymer thin film ($\sim 10 \text{ nm}$).

Table. 1 Peak position of first-order acoustic modes from Raman measurements

Au at%	TA	LA	2A	TO
0	232.31194 ± 0.86804	311.25791 ± 0.42652	458.74409 ± 1.96543	579.29365 ± 2.74366
5	232.50029 ± 1.27455	313.12214 ± 0.58209	461.6699 ± 2.35424	576.41751 ± 2.81994
20	226.48521 ± 3.64098	311.70881 ± 2.29083	475.33719 ± 8.10779	595.83984 ± 8.59915